The Prediction of Noise from Turbulent Boundary Layers Attached to Porous Media

Elisha R. Pager* and S. A. E. Miller†

University of Florida

Aerospace vehicles, wind tunnel test section walls, and other structures often contain porosity that alters the turbulent boundary layer and radiated noise. A semi-empirical mathematical model is developed to predict and analyze the acoustic radiation from turbulent boundary layers over porous media. The model is an acoustic analogy that depends on local flow-field statistics. These statistics are calculated through a steady Reynolds-averaged Navier-Stokes computational fluid dynamics solver that includes porous material. Acoustic predictions are conducted for four subsonic Mach numbers without a pressure gradient. At each Mach number, four porosities with constant liner depth and porous turbulent length scale are examined along with the non-porous solution. The flow-field is validated through comparison with acoustic measurement. Predictions are conducted to ascertain changes in acoustic radiation with varying porosity. We find that noise is amplified or reduced in a non-intuitive way with the introduction of porosity, variation of frequency, and increase of Mach number.

Nomenclature

Symbols

A_{ijlm}	Coefficient Matrix
c_∞	Ambient Speed of Sound
c_l	Streamwise Location of Velocity Profile from Leading Edge
D_p	Turbulent Length Scale
F_t	Far-field Term
f	Frequency
H	Cross-Stream Distance of the Domain
h	Liner Depth
k	Turbulent Kinetic Energy
k_p	Permeability
L	Length Scale
l_c	Scaling Coefficient for the Length Scale
P_i	Porous Inertial Tensor
P_v	Porous Viscous Tensor
R	Normalized Two-Point Cross-Correlation
S	Spectral Density
U	Free-Stream Velocity
u	Streamwise Velocity Component
$\overline{u}_c$	Local Convection Velocity
$\overline{u}_p$	Average Local Velocity
u_τ	Friction Velocity
$\mathcal{V}$	Volume
x	Streamwise Coordinate
y	Cross-Stream Coordinate
y^+	Wall Coordinate

Greek Symbols

β	Measurement Coefficient
ΔdB SPL	Change in Sound Pressure Level
Δ_1	Parameter of Integration
δ	Boundary Layer Thickness
η	Vector Between Sources
ρ	Density
μ	Dynamic Viscosity
ξ	Streamwise Source Separation
τ_w	Wall Shear Stress
ω	Radial Frequency

Non-Dimensional Numbers

uU_∞^{-1}	Non-Dimensional Velocity
X	Porosity
yH^{-1}	Non-Dimensional Height
$\mathcal{R}e_x$	Reynolds Number
$\mathcal{S}t$	Strouhal Number
$\boldsymbol{\mathcal{M}}$	Vector Mach Number

Abbreviations

CFD	Computational Fluid Dynamics
CFL	Courant-Friedrichs-Lewy Number
dB	Decibels
DNS	Direct Numerical Simulation
LES	Large Eddy Simulation
RANS	Reynolds-Averaged Navier-Stokes
SPL	Sound Pressure Level
TKE	Turbulent Kinetic Energy

*University Scholars Undergraduate Student, Department of Mechanical and Aerospace Engineering, University of Florida, P.O. Box 116250, Gainesville, FL, 32611, USA, AIAA Member, epager@ufl.edu; elisha.pager@gmail.com

†Assistant Professor, Department of Mechanical and Aerospace Engineering, University of Florida, P.O. Box 116250, Gainesville, FL, 32611, USA, AIAA Lifetime / Senior Member, saem@ufl.edu; saemiller@gmail.com

Introduction

Turbulent boundary layers are prevalent within all flows involving aerospace flight vehicles. Porous materials are becoming more prevalent on flight vehicles because they alter the flow and associated acoustic radiation. For example, porous materials are used within aircraft engines to absorb noise created by the fan. Porous materials are placed both in the inlet and outlet of the engine (see Nayfem et al.[1] for details). Porous materials are increasingly being used within wind tunnels to absorb noise in order to make more accurate aerodynamic and acoustic measurements. For example, Cobo et al.[2] shows how porous liners within the closed test section of an anechoic wind tunnel alter noise. Another purpose of porous materials within wind tunnels is to absorb the sound radiated from the turbulent boundary layer. The statistics of turbulence and radiated noise of a boundary layer attached to a porous material is different relative to a traditional boundary layer. In this paper, we quantify the alteration of the meanflow, turbulent statistics, and radiated noise relative to traditional boundary layer aerodynamics and aeroacoustics.

Multiple studies were performed to examine the changes of turbulent boundary layer statistics in the presence of permeable material. Direct numerical simulation (DNS) was performed by Breugem et al.[3] within a channel flow that contained a single permeable wall. The results from this investigation showed that the permeability of the wall led to a decrease in the viscous wall shear stress causing an increase in the skin friction in the turbulent flow regime. Turbulent boundary layers attached to porous media were also studied experimentally. Manes et al.[4] examined the effect of wall permeability within an open turbulent channel. It was found that when permeability was introduced into the wall, the no-slip condition at the wall was relaxed allowing turbulence to penetrate within the wall. This resulted in the penetration of attached eddies and the development of shear instabilities. While the goal of this experiment was to examine the near-wall turbulent structures, it also provided insight into how turbulence reacts with the porous media. As an alternative to the study of flow over porous surfaces, flow through porous material was examined experimentally by Dukhan.[5] This experiment examined the reduction of static pressure due to flow through metal foam of different porosities and pore densities. Dukhan[5] plotted pressure reduction against superficial velocity, and it was observed that the pressure drop was significantly higher for lower porosities. We selected parameters that match the experiment of Dukhan[5] because the objective of their work was important and relevant; therefore it will be used to determine what porosity and turbulent length scale to initialize our numerical simulations.

Only a few investigations were performed to study the acoustic radiation of permeable boundary layer turbulence relative to aerodynamic investigations. One canonical study is of Ffowcs-Williams,[6] who examined acoustics from turbulence near liners. Ffowcs-Williams[6] found that at low Mach numbers, the liner increased the sound radiated through additional sound scattering. Hersh[7] performed experiments to investigate the noise from a wall with surface roughness. From these experiments, Hersh[7] concluded that the efficiency of sound production increases as the boundary layer thickness decreases for a given roughness. Hersh[7] also characterized the sound generated from the turbulent boundary layer as being dipole in nature. Empirical models were used by Howe[8] to predict the correlation of surface pressure and the subsequent sound radiation for both smooth and rough walls. Howe[8] made this prediction by relating the wall wavenumber pressure spectrum to the acoustic spectrum. Turbulent boundary layers near rough walls were examined by Glegg et al.,[9] in a similar way to that of Howe,[8] by defining two additional sound sources for the noise generation. The wall wavenumber pressure spectrum was used like in Howe,[8] as well as a correlation function for the surface roughness distribution. Finally, Smith et al.[10] performed experiments to investigate the near-field pressure spectrum that is dependent on wall roughness. Smith et al.[10] concluded that wall pressure and surface roughness noise are simply related by the wall pressure spectrum, the frequency squared, and the mean-square roughness height. These studies, other than the one of Ffowcs-Williams,[6] considered wall roughness and not porosity. There is little to no experimental data available for the acoustic radiation from porous turbulent boundary layers, but some similarity can be deduced from a wall with roughness.

In the present paper, the aerodynamics and acoustics of multiple porous media zero pressure gradient turbulent boundary layers are studied. The steady Reynolds-averaged Navier-Stokes (RANS) equations are solved numerically for a range of subsonic Mach numbers. The boundary condition at the wall uses the traditional assumption of no-slip. To simulate porous media, the equations of motion are penalized in a region of constant thickness above the traditional no-slip wall boundary condition. The steady RANS solutions of both the traditional and porous wall cases are used as arguments in an acoustic analogy to predict the radiated noise. We focus on the noise radiated from the boundary layer turbulence and how porosity alters the statistics and sound source.

In the next section, we present our mathematical model to characterize porous media in the context of steady RANS and an acoustic analogy to predict noise. We present steady RANS calculations of boundary layers flowing over porous media and corresponding acoustic predictions. Finally, we summarize our findings and present our goals for future work.

Mathematical Model

Aerodynamics of the Porous Boundary Layer

The boundary layer aerodynamics are governed by the steady RANS equations closed by the Menter[11] k-ω shear stress transport turbulence model. We regard the porous region of the boundary layer flow to consist of voids that allow the fluid to move through the material. We are interested in the macroscopic behavior of the fluid within the porous media. We use the Star-CCM+ computational fluid dynamics (CFD) solver to find numerical solutions of the steady RANS equations. The momentum equation is modified with additional porous media source terms. In Star-CCM+, coefficients are used to calculate the porous source term on the right hand side of the momentum equation. Physically, the porous media alters the structure of turbulence within the media and near the wall (within the boundary layer). Integral scales of turbulence within the media and near the porous wall are proportional to the largest regions of fluid within the porous media. The length scale of turbulence in the porous material is prescribed to be proportional to the largest average diameter of fluid volume within the porous region. We focus on porous material with isotropic properties.

We use the superficial velocity formulation, and within Start-CCM+[12] it is known as porous region modeling. As the fluid enters porous media, it accelerates due to the reduction of fluid volume relative to the free-stream. The formulation is statistical and each hole within the porous material is not modeled explicitly, thus the velocity is not directly calculated within each fluid volume of the porous media. A superficial velocity is found based on the mean velocity in the fluid region and the local porosity. Within the porous region, statistics of turbulence such as length scale are prescribed because the Menter[11] closure is not enforceable. The turbulent statistics prescribed in the porous region are turbulent kinetic energy, k, and a length scale.

We now introduce the mathematical models that simulate porosity. The porosity, X, is the ratio of fluid volume to total volume within the porous medium

$$X = \frac{\mathcal{V}_{\text{fluid}}}{\mathcal{V}_{\text{total}}}, \tag{1}$$

where $\mathcal{V}_{\text{fluid}}$ is the total volume of the fluid that resides within the porous region and $\mathcal{V}_{\text{total}}$ is the total volume of the porous region. The porous model depends on relating the pressure gradient using a modified form of Darcy's law (see Huang and Ayoub[13] for details) as

$$-\nabla p = \frac{\mu}{k_p}\overline{u}_p + \beta\rho\overline{u}_p^2, \tag{2}$$

where k_p is the permeability, p is the pressure, $\overline{u}_p$ is the average local velocity within the porous media, β is a coefficient that is prescribed through measurement, and μ is the viscosity. The permeability is defined as

$$k_p = \frac{X^3 D_p}{150(1-X)^2} \tag{3}$$

and the coefficient β is

$$\beta = \frac{1.75(1-X)}{X^3 D_p}, \tag{4}$$

where D_p is the average diameter of the fluid pockets within the porous region. We elect to use a particular form of the Ergun equation, as shown by Bird,[14] that is an empirical approximation of Eqn. 2

$$-\frac{\Delta p}{L} = \frac{150\mu(1-X)^2 u_p}{X^3 D_p^2} + \frac{1.75\rho(1-X)u_p^2}{X^3 D_p}, \tag{5}$$

where L is a length scale. This pressure gradient, due to the porous material, is nonzero on the right hand side of the RANS momentum equations only within the porous material. It is set to zero within the region

where $X = 1$ (pure fluid). Here, the constants within Eqn. 5 are represented as the porous viscous resistance tensor,

$$P_v = \frac{150\mu(1-X)^2}{X^3 D_p^2}, \tag{6}$$

and the porous inertial resistance tensor,

$$P_i = \frac{1.75\rho_\infty(1-X)}{X^3 D_p}. \tag{7}$$

These terms prescribed from measurements characterize the porous material. For more detail on the porosity settings according to the CFD software see Star-CCM+.[12]

Aeroacoustics of the Turbulent Porous Boundary Layer

Predictions of the spectral density of acoustic pressure are conducted using the approach of Miller.[15] Here, the cross-spectral acoustic analogy is used, which is a statistical solution of the Navier-Stokes equations in the form of the Lighthill acoustic analogy. We retain the far-field term, as it was previously shown that the mid-field and near-field terms contribute very little acoustic energy from a subsonic turbulent boundary layer. It was shown that the spectral density of the acoustic pressure from a turbulent boundary layer with one particular form for the two-point cross-correlation of the equivalent source is

$$S(\boldsymbol{x},\omega) = 4\pi^{-2} \int_{-\infty}^{\infty} \ldots \int_{-\infty}^{\infty} \{A_{ijlm} l_{sy} l_{sz} F_t \mathcal{I}\}\, d\xi d\boldsymbol{\eta}, \tag{8}$$

where A_{ijlm} is a coefficient matrix, ξ is a vector between two sources in the axial direction, and $\boldsymbol{\eta}$ is a vector from the origin to a point within the turbulent boundary layer. The far-field term is $F_t \approx c_\infty^{-4} r^{-1} r'^{-1}$. The coefficient matrix is $A_{ijlm} \approx \overline{\rho}\ \overline{\rho' \overline{u_i u_j}}\ \overline{u_l' u_m'}$.

Integrations are performed by choosing a Gaussian based decay model of the normalized two-point cross-correlation of the equivalent source, R. Here, R is dependent on the steady RANS solutions with and without a porous surface. Within Eqn. 8, $\mathcal{I}$ is shown in Miller,[15] and is the result of analytical integration of the two-point cross-correlation model.

The length scales of the flow are estimated using the approach of Efimtsov.[16] We select a set of coefficients, a_i, within the model of Efimtsov,[16] to approximate both the streamwise and cross-stream length scale. The length scale is dependent on the local convection velocity, which is estimated to be $\overline{u}_c = 0.70\overline{u}$.

We numerically evaluate Eqn. 8 by approximating the integrals in the ξ and η directions, which are the streamwise and cross-stream directions, respectively. A mirror source, following the approach of Powell,[17] is used to account for the reflection of acoustic waves at the wall. Observer positions, $\boldsymbol{x}$, are restricted to regions above the boundary layer thickness. Numerical integration is performed by using the boundary layer profile derived from the steady RANS solution. We do not evaluate Eqn. 8 within the porous region.

Results

Aerodynamics

Each steady RANS solution is obtained after 100,000 and 600,000 iterations of the solver for the non-porous and porous boundary layers, respectively. The Courant-Friedrichs-Lewy (CFL) number is held constant at 20 for each boundary layer flow, except for $\mathcal{M} = 0.3$, where a time step ramping is required for convergence. The CFL number is 0.5 for the first 100,000 iterations and then increased to 45 for the remaining iterations. A grid independence study is performed for both the porous and the non-porous domain. The aerodynamic drag at the wall is used to help demonstrate convergence and grid-independence. The grid independence study is shown in Fig. 1.

The domain is a rectangle with appropriate boundary conditions on each side. We discuss the specification of the boundary conditions later. The non-porous domain is shown in Fig. 2 and the porous domain is shown in Fig. 3. For the porous boundary layer predictions two separate spatial regions, the non-porous region and the porous region, are defined as previously discussed in the modeling section. The porous region of the

domain consists of a sub-domain, which is adjacent to the no-slip wall and extends from $x = 0$ m to $x = 3$ m. We examine a porous region with a constant depth of 0.1 m and a constant turbulent length scale of 0.3 mm. The length scale is selected based on the experiment of Dukhan.[5] Within the porous region that resides within the lower half plane of the domain, we specify the porosity, porous inertial resistance tensor, porous viscous resistance tensor, and the turbulent length scale. The porosity, porous tensors, turbulent length scale, liner depth, and Mach number for each of the twenty boundary layers investigated are shown in Table 1.

Boundary conditions of the porous and non-porous boundary layers are consistent at the inflow, outflow, and free-stream. The boundary conditions on the wall of the domain require a separate treatment for porous and non-porous flows. Flow enters the domain on the left boundary. A subsonic inflow is enforced, at $x = -1$ m, by specifying the total pressure and temperature corresponding to the inflow Mach number. The flow exits the domain at the right boundary. Here, a static pressure outlet is imposed through specification of the ambient static pressure. The ambient pressure and temperature for each corresponding Mach number investigated are normalized and listed in Table 2. At the top of the computational domain, $y = 1$ m, a free-stream boundary condition is specified.

At the wall of the computational domain, from $x = -1$ m to $x = 0$ m and $y = 0$ m, a symmetry or slip-wall is enforced to allow variation of the streamwise velocity component. At the solid wall boundary, $y = 0$ m and $x > 0$ m, a no-slip adiabatic wall is specified for traditional non-porous turbulent boundary layer calculations. An alternative boundary condition and domain are used for porous boundary layer calculations. An internal boundary condition interface between the two regions joining at $y = 0$ m and $x > 0$ m is created for the flow to pass through. This interface separates the porous and non-porous regions of the fluid. Within the porous region, we set $D_p = 0.3$ mm and $X = 0.8, 0.85, 0.9$, and 0.95 (for the porous cases examined) based on the experiment of Dukhan.[5] The porous tensors are determined according to Eqns. 6 and 7.

The steady RANS simulations exhibit both consistency and stability, and we examine convergence through tracking residuals of the governing equations as a function of iteration. In Figs. 4 and 5, the residuals of the $\mathcal{M}_\infty = 0.5$ non-porous and $X = 0.95$ solutions are shown. The y-axis represents the field-variable or turbulent statistic residual, and the x-axis represents the iteration. Each simulation of porous and non-porous turbulent boundary layers show similar behavior of the residual. The residuals approach a constant value after 100,000 iterations for non-porous cases and 500,000 to 800,000 iterations for porous cases. Generally, the normalized residuals are lowered by three to five orders of magnitude, per simulation. For the low-speed, $\mathcal{M}_\infty = 0.3$ cases, more iterations are required for convergence. The non-porous cases required approximately 100,000 iterations to reach convergence, and the porous cases required approximately 600,000 iterations to reach convergence.

We now examine the contours of $\mathcal{M} = \overline{uc}^{-1}$, shown in Figs. 6 and 7. In both figures, the x-axis is the streamwise direction and the y-axis is the cross-stream direction of the flow. In Fig. 6, the flow corresponds to $\mathcal{M} = 0.9$ and $X = 1$, the non-porous wall, and in Fig. 7 the flow corresponds to $\mathcal{M} = 0.9$ and $X = 0.9$. We derive our profile statistics from the location $x_l = 1$ m, because this is the location Gloerfelt[18] used in a large eddy simulation study of boundary layer turbulence and noise. These simulations assume fully turbulent flow starting at the leading edge of the no-slip wall at $x = y = 0$ m.

We now examine the derivation of numerical quantities from the steady RANS solutions that are closed by the $k-\omega$ Menter SST model. These numerical quantities are parameters needed to quantify the turbulent boundary layer and subsequently predict the acoustic radiation. Table 3 shows the theoretically derived flow properties for the non-porous solution. These values are used as guidelines to simulate the correct flow inside the domain. Table 4 shows numerically derived flow properties for the non-porous solutions, and they are based on $\mathcal{M}_\infty$, $\mathcal{R}e_x$, and the profile location of $x = 1$ m. We derive the shear stress at the wall, τ_w, the boundary layer thickness, δ, the friction velocity u_τ, and the distance from the wall to the first grid point, Δy_1. These same quantities are derived for the porous solutions in Table 5. These boundary layer flow properties are found through similar approaches except for the frictional velocity. For a one-to-one comparison between the porous and non-porous steady RANS solutions, we require that u_τ be the same at each $\mathcal{M}$. We set u_τ for the porous cases to be equal to the non-porous cases for analysis purposes only. It is observed in our numerical solutions that introducing porosity at the wall results in a decrease in wall shear stress, and an increase in the boundary layer thickness.

We now examine quantitative comparisons of the steady RANS solutions. Figure 8 shows the mean velocity profile in outer coordinates for $\mathcal{M} = 0.3$, 0.5, 0.7, and 0.9. The non-porous solution is represented by the solid black line, and the porous solutions are represented by the other lines. The x-axis is the non-

dimensional height, yH^{-1}, where y is the cross-stream coordinate and H is the cross-stream distance within the domain. The y-axis is uU_∞^{-1}, where the streamwise velocity component is normalized by the free-stream velocity. It is observed that the porous boundary layers contain higher velocities relative to the non-porous boundary layers. We expect this result as high-speed flow induces larger flow velocities within the porous media and at the wall. The velocity increase is consistent among all four Mach numbers investigated. An interesting trend is observed amongst all four Mach numbers and four porosities. As porosity of the wall decreases (the wall becomes more fluid), the velocity decreases to the velocity of the non-porous wall. This is due to the smaller volumes of porous media that effectively accelerates the flow within the wall. It is also observed that the boundary layer thickness decreases for porous boundary layer flows.

We now examine the turbulent kinetic energy (TKE), k, of the boundary layer for the non-porous and porous cases in outer coordinates. The plots of Fig. 9 represent the variation in k as a function of dimensionless height, yH^{-1}. The TKE is normalized by the ambient speed of sound squared, c_∞^2, on the y-axis and the dimensionless height is the same as in Fig. 8. Generally, as $\mathcal{M}$ increases k increases. The TKE is highly impacted by $\mathcal{M}$ and porosity relative to the meanflow. The same reverse trend that is observed in the mean velocity of the flow is also observed in the TKE. As porosity decreases (the wall contains more fluid), the TKE increases to the TKE of the non-porous wall. This trend is observed at all four Mach numbers, but as $\mathcal{M}$ decreases so does the value of k. We attribute this non-intuitive trend to the higher acceleration within more-so porous materials, which in turn reduces the shear (and therefore production of TKE) within the boundary layer.

The variation in the meanflow and the turbulent kinetic energy has been examined for both the non-porous and porous turbulent boundary layers. In these numerical simulations, we have shown that at each Mach number investigated the same trends are followed by the mean velocity profile and the TKE. Recall that in these simulations $X = 0.80, 0.85, 0.90, 0.95$, and 1, where $X = 1$ represents a solid wall. We will now use these steady RANS simulations to predict the acoustic radiation from the non-porous and porous boundary layers.

Aeroacoustics

We now evaluate Eqn. 8 to predict acoustic radiation from the non-porous and porous turbulent boundary layers. We calibrate the coefficients of Eqn. 8 with a single non-porous steady RANS solution of the Star-CCM+ solver and the prediction of Gloerfelt.[18] Measuring noise from turbulent boundary layers is very difficult due to the background noise of wind-tunnels. For this reason, we compare our predictions with the well-validated prediction method of Gloerfelt,[18] which is based on LES. The scaling coefficient of the length scale is adjusted to match the LES predictions of Gloerfelt[18] for a single case. We set the value of $l_c = 2.0$. The coefficient is held constant and never changed after this calibration.

We compare acoustic predictions of the non-porous turbulent boundary layer with those of Gloerfelt.[18] These comparisons are shown in Fig. 10, where the y-axis is sound pressure level (SPL) per unit Hertz and the x-axis is frequency, f, in Hertz. These predictions are based on the extracted steady RANS profile at $x = 1$ m. The scaling at low frequencies, near $f \approx 1000$ Hz, agrees with the LES results of Gloerfelt.[18] At higher frequencies, $f > 30$ kHz, the fall-off of SPL with f also agrees with LES. The magnitude of the prediction in this high frequency range does not show as good agreement with LES.

We now examine acoustic radiation from the porous turbulent boundary layers. Predictions are shown in Fig. 11, where the y-axis is the change in sound pressure level (ΔdB SPL) per unit Hertz, and the x-axis is frequency, f, in Hertz. We show changes in SPL relative to the corresponding baseline non-porous turbulent boundary layer. The change in SPL is represented as the difference of the non-porous and each porous boundary layer, $\Delta\text{SPL} = \text{SPL}_{\text{non-porous}} - \text{SPL}_{\text{porous}}$. Like before, these predictions are based on the steady RANS profile at $x = 1$ m. At frequencies $f \approx 1000$ Hz and Mach numbers $\mathcal{M}_\infty = 0.7$ and 0.9, the predicted SPL is lower than that of the non-porous case. This is represented by a positive ΔdB value in Figs. 11(c) and 11(d). However, at $\mathcal{M}_\infty = 0.3$ and 0.5 a few of the predicted porous SPL are higher than that of the non-porous case, which is represented as a negative ΔdB value in Figs. 11(a) and 11(b). At $\mathcal{M}_\infty = 0.5$ and $X = 0.8$, the SPL increases compared to the non-porous prediction. At $\mathcal{M}_\infty = 0.3$ and $X = 0.8$, the SPL also increases compared to the non-porous solution. There is also a reverse trend of the acoustic results that corresponds to the meanflow and TKE results. As porosity decreases from $X = 0.95$ (for all Mach numbers examined) the change in SPL, ΔdB SPL, decreases. This trend demonstrates that there is a range of porosity that produces less acoustic radiation. As X decreases, the change in SPL approaches the non-porous result. This trend is a direct result of TKE decreasing as porosity increases. The SPL produced from the boundary

layer is highly dependent on the TKE within the boundary layer. The fall-off of the porous boundary layer SPL occurs at a much higher rate relative to the non-porous boundary layer. The large peaks of ΔSPL in Fig. 11 represent the change where the SPL drops-off when compared to the non-porous solution. In each porous boundary layer flow, the spectra shift to lower frequencies. Likewise, the spectra shifts to lower SPL with increasing $\mathcal{M}_\infty$.

Summary and Conclusion

We presented numerical predictions of the changes in acoustic pressure from non-porous and porous turbulent boundary layers to quantify noise reduction. We presented predictions for four porosities at a single porous material depth and turbulent length scale corresponding to $X = 0.80, 0.85, 0.90$, and 0.95, $h = 0.1$ m, and $D_p = 0.3$ mm at four Mach numbers. These porosities and associated parameters are chosen based on the experimental investigation of Dukhan.[5]

The mean velocity profiles contain large differences near the wall for all Mach numbers investigated. The porous velocity profiles are higher at the wall, which is expected due to the accelerated velocity induced by the porous media. This is due to the lack of the no-slip condition and lower shear layer gradient in the cross-stream direction. As porosity decreases, more fluid resides within the porous region, and the velocity decreases and approaches the non-porous profile. In addition to meanflow profiles, TKE is examined, and found to vary greatly with the addition of porous material. Within porous turbulent boundary layers, TKE falls by almost half of the non-porous TKE for $X = 0.8$ and $\mathcal{M}_\infty = 0.3, 0.5, 0.7$, and 0.9. As Mach number increases, it is shown that mean velocity and TKE of the non-porous turbulent boundary layer increase. As porosity decreases and the wall contains more fluid, the TKE increases. The same trend is observed for the porous turbulent boundary layer, but the velocity is larger while the TKE is relatively lower. We explain this trend as a result of larger accelerations within the more porous materials causing a reduction in the shear within the boundary layer.

The acoustic trends with varying porosity are consistent across Mach numbers. The high frequency fall-off of the SPL starts at consistently lower frequencies relative to the non-porous boundary layers. The porous SPL falls-off at a frequency of approximately 700 Hz while the non-porous SPL falls off at approximately 10 kHz. Trends of ΔSPL vary depending on the Mach number. Generally, the change in ΔSPL decreases as Mach number decreases. As porosity decreases the change in ΔSPL also decreases at each Mach number. For lower Mach numbers such as $\mathcal{M}_\infty = 0.30$ and $\mathcal{M}_\infty = 0.50$, SPL actually increases for porosities lower than $X = 0.85$. For example, at $\mathcal{M}_\infty = 0.90$ and $X = 0.80$ the porous SPL decreases by approximately 4 dB and at $\mathcal{M}_\infty = 0.3$ and $X = 0.80$ the porous SPL increases by approximately 3 dB for all frequencies. In general, the noise produced by the boundary layer turbulence is lowered for values of X approaching unity. As the noise produced by porous boundary layer turbulence approaches the solid wall case (X approaches smaller values) the ΔSPL approaches zero.

Our predictions and theory would benefit from careful experiments, and experiments would validate the unique acoustic trends predicted within this research. In general, there is a lack of measurements on turbulent boundary layers that contain porosity and associated radiated noise.

Acknowledgments

The University of Florida University Scholars Program provided funding for the first author.

References

[1]Nayfeh, A. H., Kaiser, J. E., and Telionis, D. P., "Acoustics of Aircraft Engine-Duct Systems," *AIAA Journal*, Vol. 13, No. 2, 1975, pp. 130–153. doi:10.2514/3.49654.

[2]Cobo, P., Ruiz, H., and Alvarez, J., "Double-Layer Microperforated Panel/Porous Absorber as Liner for Anechoic Closing of the Test Section in Wind Tunnels," *Acta Acustica united with Acustica*, Vol. 96, 2010, pp. 914–922. doi:10.3813/AAA.918350.

[3]Breugem, W. P., Boersma, B. J., and Uittenbogaard, R. E., "The Influence of Wall Permeability on Turbulent Channel Flow," *Journal of Fluid Mechanics*, Vol. 562, Aug 2006, pp. 35–72. doi:10.1017/s0022112006000887.

[4]Manes, C., Poggi, D., and Ridolfi, L., "Turbulent Boundary Layers Over Permeable Walls: Scaling and Near-Wall Structure," *Journal of Fluid Mechanics*, Vol. 687, Oct 2011, pp. 141–170. doi:10.1017/jfm.2011.329.

[5]Dukhan, N., "Correlations for the Pressure Drop for Flow Through Metal Foam," *Experiments in Fluids*, Vol. 41, No. 4, Aug 2006, pp. 665–672. doi:10.1007/s00348-006-0194-x.

[6]Ffowcs-Williams, J. E., "The Acoustics of Turbulence Near Sound-Absorbent Liners," *Journal of Fluid Mechanics*, Vol. 51, No. 04, Feb 1972, pp. 737. doi:10.1017/s0022112072001338.

[7]Hersh, A., "Experimental Investigation of Surface Roughness Generated Flow Noise," *8th Aeroacoustics Conference*, American Institute of Aeronautics and Astronautics, Apr 1983. doi:10.2514/6.1983-786.

[8]Howe, M. S., "Surface Pressures and Sound Produced by Turbulent Flow Over Smooth and Rough Walls," *The Journal of the Acoustical Society of America*, Vol. 90, No. 2, Aug 1991, pp. 1041–1047. doi:10.1121/1.402292.

[9]Glegg, S., Devenport, W., Grissom, D., and Smith, B., "Rough Wall Boundary Layer Noise: Theoretical Predictions," *13th AIAA/CEAS Aeroacoustics Conference (28th AIAA Aeroacoustics Conference)*, American Institute of Aeronautics and Astronautics, May 2007. doi:10.2514/6.2007-3417.

[10]Smith, B., Alexander, W., Devenport, W., Glegg, S., and Grissom, D., "The Relationship Between Roughness Noise and the Near-Field Pressure Spectrum," *14th AIAA/CEAS Aeroacoustics Conference (29th AIAA Aeroacoustics Conference)*, American Institute of Aeronautics and Astronautics, May 2008. doi:10.2514/6.2008-2904.

[11]Menter, F. R., "Two-Equation Eddy-Viscosity Turbulence Models for Engineering Applications," *AIAA Journal*, Vol. 32, No. 8, Aug 1994, pp. 1598–1605. doi:10.2514/3.12149.

[12]Siemens Corporation, "STAR CCM+ Users Manual," Sept 2017.

[13]Huang, H. and Ayoub, J., "Applicability of the Forchheimer Equation for Non-Darcy Flow in Porous Media," *SPE Journal*, Vol. 13, No. 1, March 2008, pp. 112–122. doi:10.2118/102715-PA.

[14]Bird, R. B., "Transport Phenomena," *Applied Mechanics Reviews*, Vol. 55, No. 1, 2002, pp. R1–R4.

[15]Miller, S. A. E., "Prediction of Turbulent Boundary-Layer Noise," *AIAA Journal*, Vol. 55, No. 5, May 2017, pp. 1659–1672. doi:10.2514/1.j055087.

[16]Efimtsov, B. M., "Characteristics of the Field of Turbulent Wall Pressure Fluctuations at Large Reynolds Numbers," *Soviet Physics Acoustics*, Vol. 28, No. 4, 1982, pp. 289–292.

[17]Powell, A., "Aerodynamic Noise and the Plane Boundary," *Journal of the Acoustical Society of America*, Vol. 32, No. 8, 1960, pp. 982–990. doi:10.1121/1.1908347.

[18]Gloerfelt, X. and Margnat, F., "Effects of Mach Number on Boundary Layer Noise," *20th AIAA/CEAS Aeroacoustics Conference*, American Institute of Aeronautics and Astronautics, June 2014. doi:10.2514/6.2014-3291.

Tables

Table 1. Porosity Cases Investigated

$\mathcal{M}_\infty$	X	h [m]	D_p [m]	P_i	P_v
0.3	0.80	0.0	0	274.64	23.694
0.3	0.85	0.1	0.003	171.73	11.111
0.3	0.90	0.1	0.003	96.446	4.1602
0.3	0.95	0.1	0.003	41.002	0.8843
0.3	1.00	0.0	0	0	0
0.5	0.80	0.0	0	274.64	23.694
0.5	0.85	0.1	0.003	171.73	11.111
0.5	0.90	0.1	0.003	96.446	4.1602
0.5	0.95	0.1	0.003	41.002	0.8843
0.5	1.00	0.0	0	0	0
0.7	0.80	0.0	0	274.64	23.694
0.7	0.85	0.1	0.003	171.73	11.111
0.7	0.90	0.1	0.003	96.446	4.1602
0.7	0.95	0.1	0.003	41.002	0.8843
0.7	1.00	0.0	0	0	0
0.9	0.80	0.0	0	274.64	23.694
0.9	0.85	0.1	0.003	171.73	11.111
0.9	0.90	0.1	0.003	96.446	4.1602
0.9	0.95	0.1	0.003	41.002	0.8843
0.9	1.00	0.0	0	0	0

Table 2. Steady RANS Ambient Flow Conditions.

$\mathcal{M}_\infty$	$P_t P_\infty^{-1}$	$T_t T_\infty^{-1}$
0.30	1.06443	1.01800
0.50	1.18621	1.05000
0.70	1.38710	1.09800
0.90	1.69130	1.16200

Table 3. Theory Based Flow Conditions.

$\mathcal{M}_\infty$	$\mathcal{R}e_x$	x_l [m]	τ_w [Pa]	δ [m]	u_τ [ms^{-1}]	Δy_1 Distance [m]
0.30	6.815×10^6	1	20.43	3.073×10^{-2}	4.12	3.667×10^{-6}
0.50	1.137×10^7	1	53.24	2.976×10^{-2}	6.65	2.271×10^{-6}
0.70	1.592×10^7	1	100.2	2.916×10^{-2}	9.12	1.656×10^{-6}
0.90	2.046×10^7	1	160.7	2.872×10^{-2}	11.55	1.307×10^{-6}

Table 4. Numerically Derived Flow Properties for Non-Porous Conditions.

$\mathcal{M}_\infty$	$\mathcal{R}e_x$	x_l [m]	τ_w [Pa]	δ [m]	u_τ [ms^{-1}]	Δy_1 Distance [m]
0.30	6.815×10^6	1	43.25	4.886×10^{-2}	4.04	3.737×10^{-6}
0.50	1.137×10^7	1	112.2	1.357×10^{-3}	6.87	2.199×10^{-6}
0.70	1.592×10^7	1	211.5	1.631×10^{-3}	10.8	1.395×10^{-6}
0.90	2.046×10^7	1	340.9	1.912×10^{-3}	12.4	1.218×10^{-6}

Table 5. Numerically Derived Flow Properties for Porous Conditions.

$\mathcal{M}_\infty$	$\mathcal{R}e_x$	x_l [m]	τ_w [Pa]	δ [m]	u_τ [ms^{-1}]	Δy_1 Distance [m]
0.30	6.815×10^6	1	1.936×10^{-3}	1.025×10^{-1}	4.04	3.737×10^{-6}
0.50	1.137×10^7	1	3.053×10^{-3}	1.006×10^{-1}	6.87	2.199×10^{-6}
0.70	1.592×10^7	1	3.053×10^{-3}	1.006×10^{-1}	10.8	1.395×10^{-6}
0.90	2.046×10^7	1	3.053×10^{-3}	1.006×10^{-1}	12.4	1.218×10^{-6}

Figures

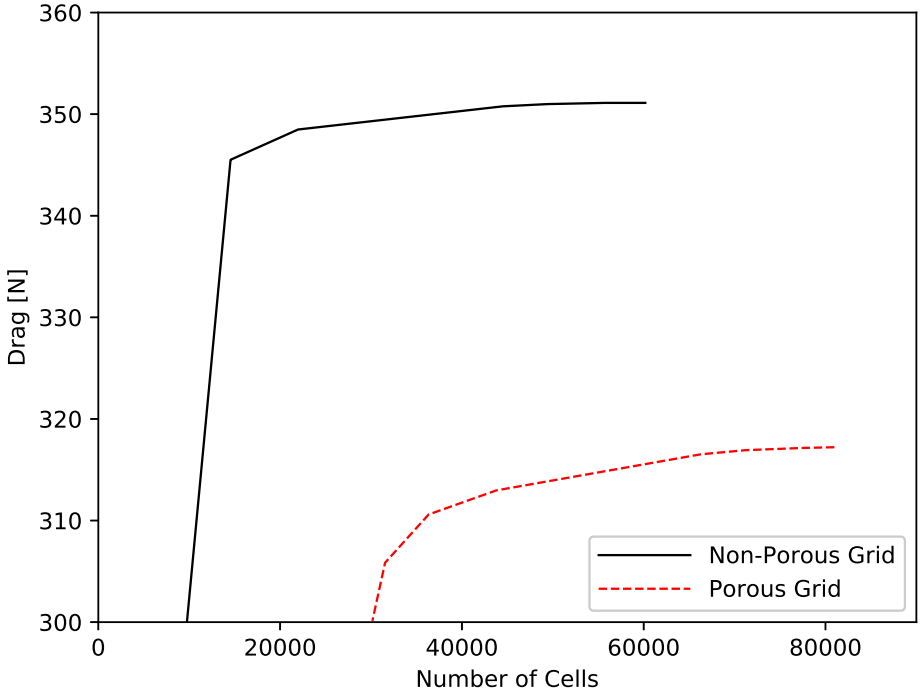

Figure 1. Grid independence study for the non-porous and porous grids.

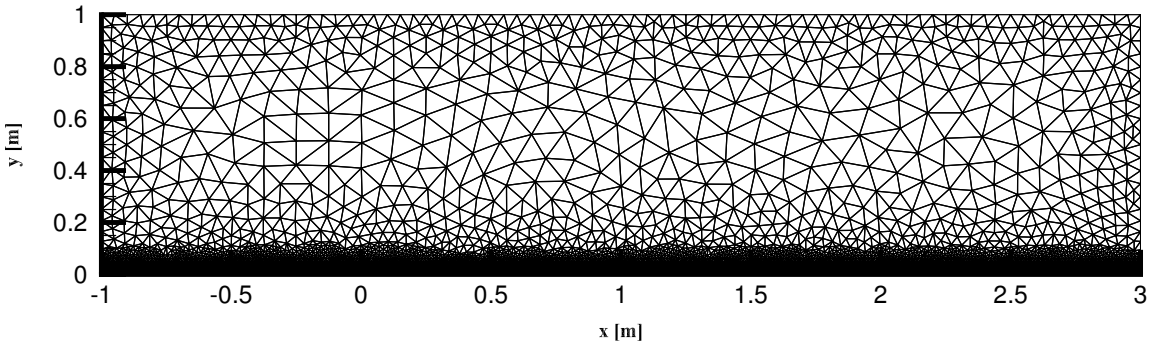

Figure 2. The non-porous computational domain.

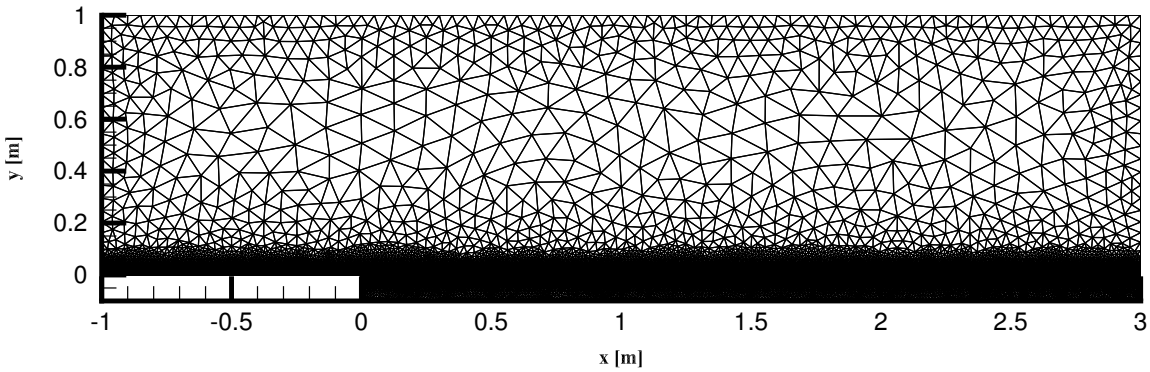

Figure 3. The porous computational domain.

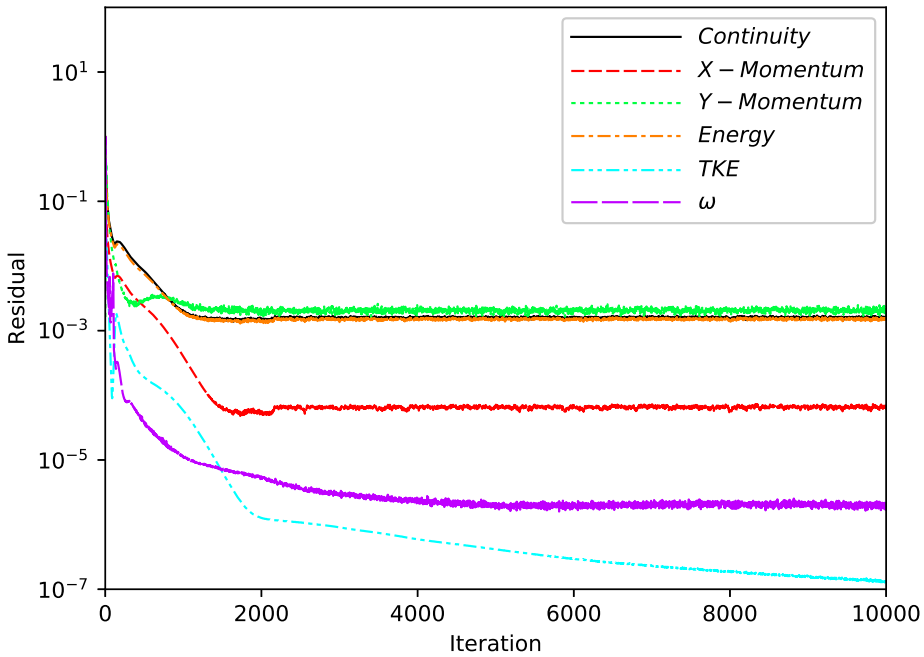

Figure 4. Variation of residual of field-variables for $\mathcal{M}_\infty = 0.5$ and $X = 1$.

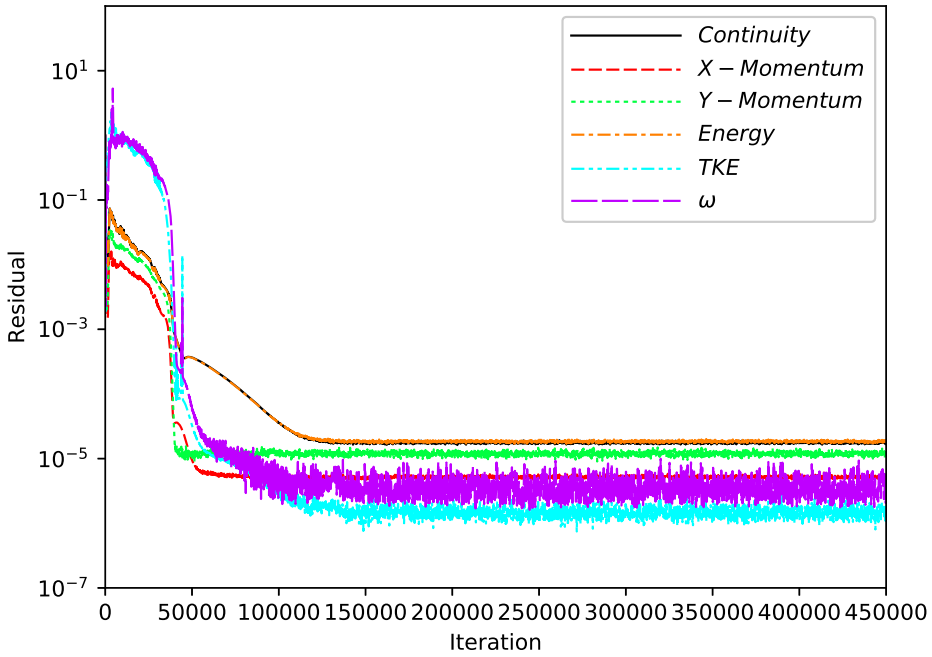

Figure 5. Variation of residual of field-variables for $\mathcal{M}_\infty = 0.5$ and $X = 0.95$.

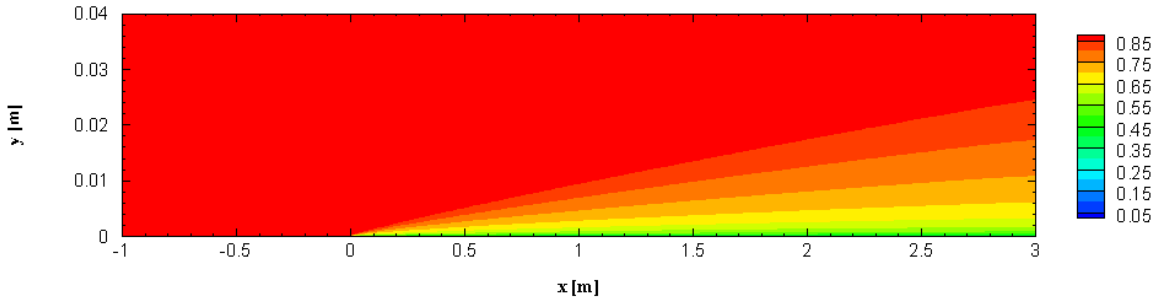

Figure 6. Contours of $\mathcal{M} = \overline{uc}^{-1}$ for $\mathcal{M}_\infty = 0.9$ and $X = 1$.

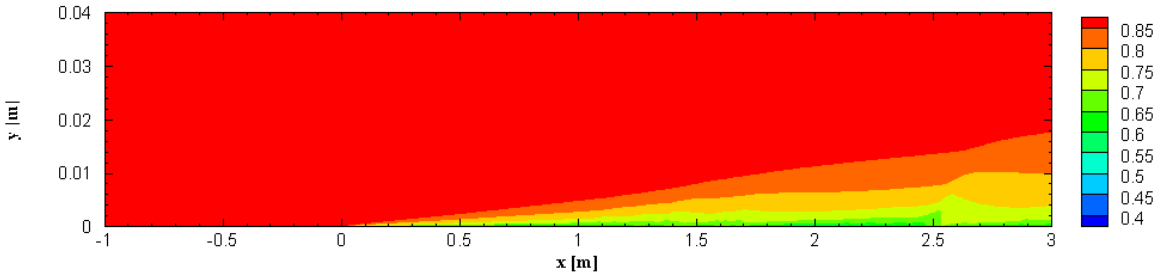

Figure 7. Contours of $\mathcal{M} = \overline{uc}^{-1}$ for $\mathcal{M}_\infty = 0.9$ and $X = 0.9$.

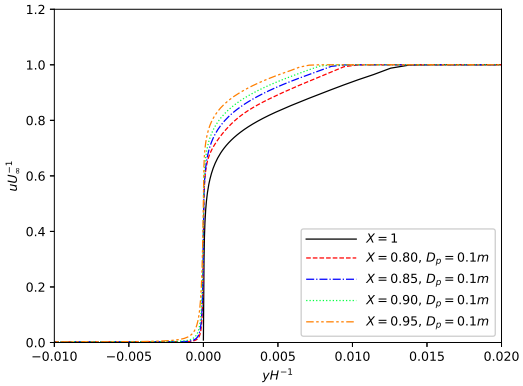

(a) $\mathcal{M}_\infty = 0.30$

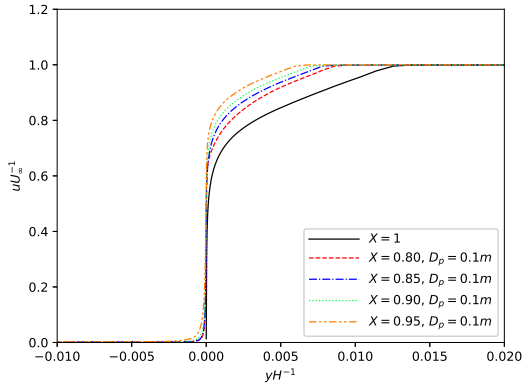

(b) $\mathcal{M}_\infty = 0.50$

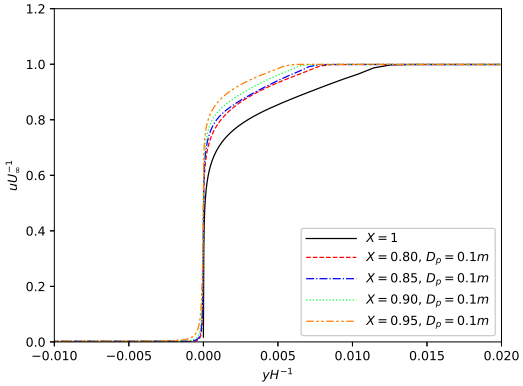

(c) $\mathcal{M}_\infty = 0.70$

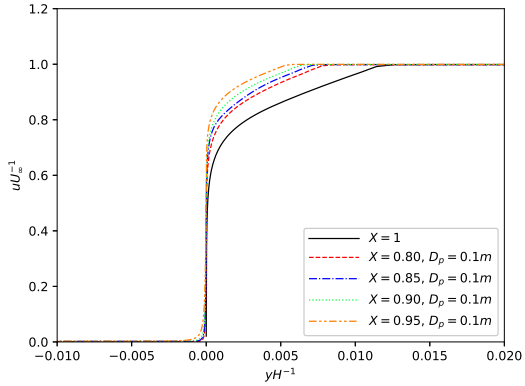

(d) $\mathcal{M}_\infty = 0.90$

Figure 8. Mean-velocity profile in outer coordinates normalized by the free-stream velocity and presented as a function of dimensionless height yH^{-1}.

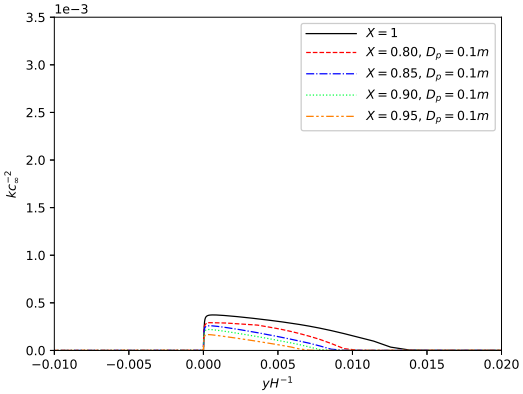

(a) $\mathcal{M}_\infty = 0.30$

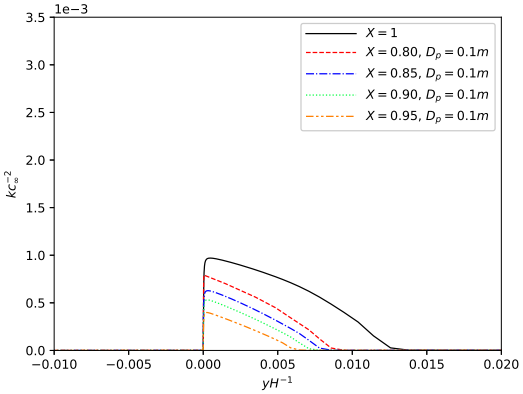

(b) $\mathcal{M}_\infty = 0.50$

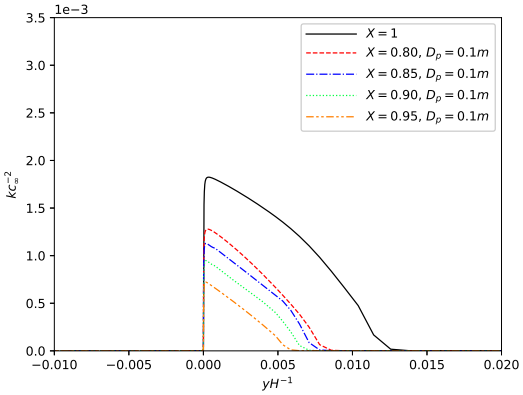

(c) $\mathcal{M}_\infty = 0.70$

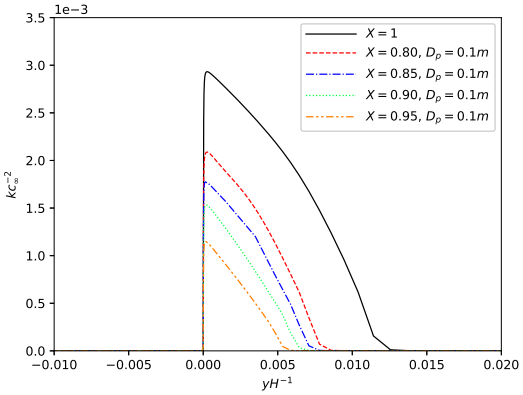

(d) $\mathcal{M}_\infty = 0.90$

Figure 9. Turbulent kinetic energy in outer coordinates normalized by the ambient speed of sound squared, c_∞^2.

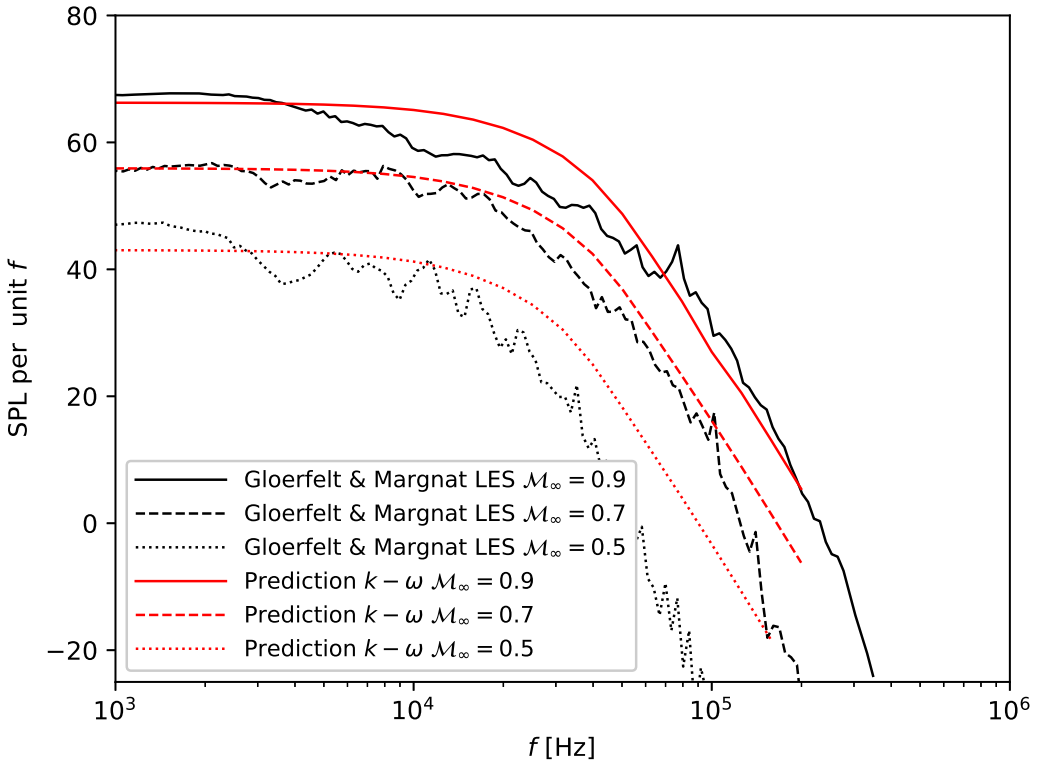

Figure 10. Predictions compared to LES predictions of Gloerfelt and Margnat at various Mach numbers.

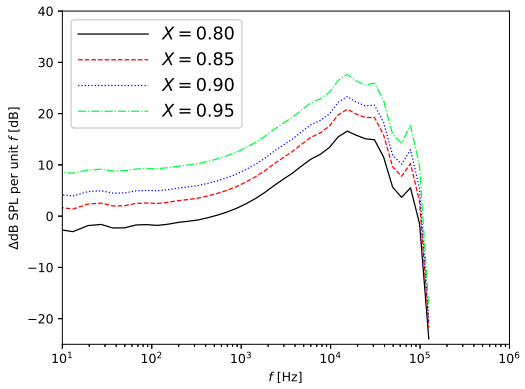

(a) $\mathcal{M}_\infty = 0.30$

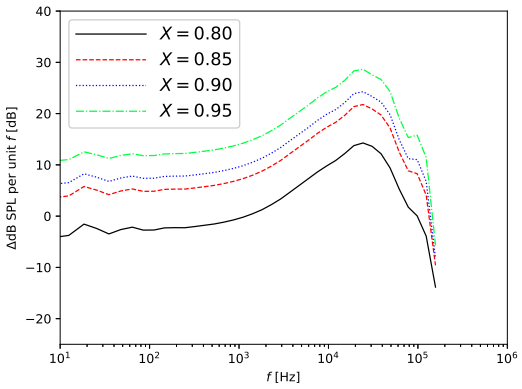

(b) $\mathcal{M}_\infty = 0.50$

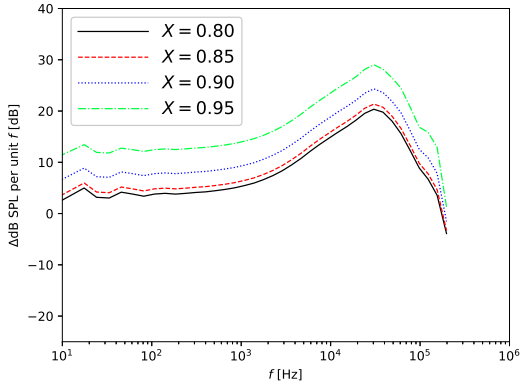

(c) $\mathcal{M}_\infty = 0.70$

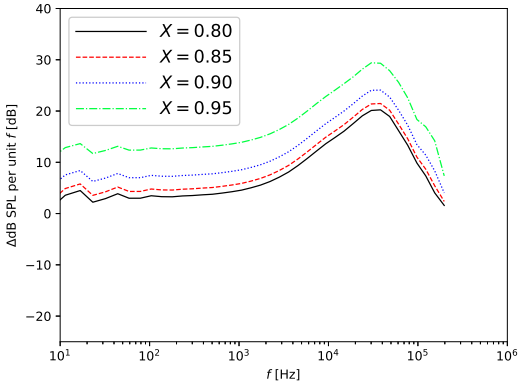

(d) $\mathcal{M}_\infty = 0.90$

Figure 11. Predictions of ΔdB SPL per unit f for four porous wall turbulent boundary layers. Positive ΔSPL represents noise reduction relative to the solid wall case.